

# The influence of overall texture on the grain boundary network in an AZ31 alloy

Hossein Beladi<sup>1,\*</sup>, Alireza Ghaderi<sup>1,a</sup>, Vahid Tari<sup>2</sup>, Anthony D. Rollett<sup>3</sup>, Gregory S. Rohrer<sup>3</sup>

<sup>1</sup> Institute for Frontier Materials, Deakin University, Geelong, Victoria 3216, Australia

<sup>2</sup> ATI Specialty Materials, Monroe, NC, 28111, USA

<sup>3</sup> Department of Materials Science and Engineering, Carnegie Mellon University, Pittsburgh, PA 15213-3890, USA

\* Corresponding Author: Hossein Beladi

hossein.beladi@deakin.edu.au

Accepted for publication, Metallurgical and Materials Transactions A, 2025

## Abstract

Three samples of an AZ31 alloy with distinct textures were produced through chill casting, hot extrusion and hot rolling. The as-cast material exhibited a relatively random texture, while the hot extruded and hot rolled materials displayed  $\{hki0\}$  prism and (0001) basal textures, respectively. This also led to significant differences in the characteristics of their grain boundary networks (i.e., the distribution of misorientations and plane orientations). The misorientation angle distribution of as-cast condition was similar to a random distribution. However, the other processing routes were significantly different from random, displaying a pronounced peak at  $\sim 30^\circ$  misorientation angle, beyond which the distribution differed depending on the processing condition. Synthetically generated orientations belonging to each texture had misorientation angle distributions comparable to those measured for each processing route. This confirmed that the texture characteristics dictate the population of boundary misorientations. The distribution of grain boundary planes was anisotropic for all conditions, though the extent of anisotropy and their distribution characteristics depended on the processing route. It appeared that the relative areas of the grain boundary planes are largely influenced by the characteristics of the overall texture, where the hot rolling process promoted the (0001) basal plane orientation, while the  $\{hki0\}$  prismatic plane orientation, which does not necessarily have low energy, was dominant for the hot extrusion condition.

**Keywords:** grain boundary network, processing route, texture, AZ31, five-parameter characterisation

---

<sup>a</sup> Former Research Engineer at Deakin University and currently works at 3M in St Paul, USA as a surface scientist.

## 28 **Introduction**

29 Magnesium alloys are widely used for applications requiring low density combined with moderate  
30 strength (e.g., automotive). However, they have low formability/ductility at ambient temperature due to  
31 the limited active slip systems (i.e., non-basal slip) operating upon straining [1, 2]. In turn, this promotes  
32 mechanical twinning as a dominant deformation mechanism in Mg alloys [2]. The grain boundaries  
33 appear as preferential sites for mechanical twinning nucleation because they are comprised of  
34 dislocation/defect aggregates and the presence of an abrupt change in orientation leads to high stress  
35 concentrations to maintain compatibility upon straining [3].

36 Grain boundaries have anisotropic characteristics, defined by the atomic structure between two adjoining  
37 grains and the grain boundary plane character [4-6]. Hence, the propensity of mechanical twinning  
38 nucleation differs among different grain boundaries, depending on their characteristics [3, 7, 8]. For  
39 hexagonal close-packed materials (e.g., Mg [8] and Ti [3] alloys), it was demonstrated that the  
40 mechanical twins largely nucleate on boundaries with low misorientation angles in a range of 5-10°,  
41 beyond which the propensity of mechanical twinning nucleation progressively decreases to such an  
42 extent that they are barely observed at boundaries with misorientation angles higher than 50° [8]. This  
43 suggests that the formability of magnesium alloys (i.e., retarding the mechanical twinning formation)  
44 can, to some extent, be manipulated through control of their grain boundary network, a principle known  
45 as grain boundary engineering.

46 The concept of grain boundary engineering was introduced in mid-1980s, largely focusing on austenitic  
47 metals having the face centred cubic structure [9]. Since then, several approaches have been developed  
48 to design grain boundary networks in a wide range of polycrystalline materials and ultimately enhance  
49 their material performance. These approaches consisted of iterative recrystallisation [10], changing the  
50 mechanism of phase transformation (i.e., diffusion vs shear) [11-13], varying alloy composition  
51 [10,11,14], utilising variant selection [11,14-16], and overall texture modification [13, 17-21]. Among  
52 these methods, the influence of overall orientation texture is the most applicable to magnesium alloys, as  
53 they are readily manufactured through different processing routes, ultimately altering their overall  
54 texture. However, it is not clear how the change in the overall orientation texture alters the grain boundary  
55 network of magnesium alloys.

56 The current investigation examined the impact of overall texture on the characteristics of the grain  
57 boundary networks (i.e., the distribution of misorientations and plane orientation) in an AZ31 Mg alloy.  
58 Here, the alloy was produced through different routes, namely chill casting, hot extrusion and hot rolling,  
59 leading to three distinct overall textures. The grain boundary characteristics produced by different

60 processing conditions were evaluated using electron backscatter diffraction along with the automated  
61 stereological grain boundary interpretation known as the five-parameter characterisation method [6]. The  
62 results were then interpreted using a calculation of the misorientation angle distribution resulting from  
63 synthetically generated orientations for a given overall texture.

#### 64 **Experimental procedure:**

65 An AZ31 magnesium alloy with a nominal composition of Mg-2.8 Al- 0.83 Zn- 0.45 Mn (in wt%) was  
66 received in different forms, namely cast ingot and 5 mm thick hot rolled plate. The latter is typically  
67 produced at a temperature range of 300 to 450 °C at a reduction of 10 to 30% per pass [22]. The hot  
68 rolled plate was used in the as-received condition, hereafter called the hot-rolled sample. However, the  
69 former was subjected to two different processing routes, as follows.

70 - *Chill Casting:* The as-received cast ingot was remelted at 800 °C in a stainless-steel crucible, and then  
71 solidified in a chill mould with a dimension of 100 × 20 × 20 mm<sup>3</sup> under argon gas, to reduce the  
72 formation of columnar dendrites upon solidification. The cast block was scalped to remove the chill zone  
73 near the casting surface. The material was then annealed at 450 °C for 16 h under inert gas (hereafter  
74 called the as-cast condition) to remove any mechanical twins, which might be introduced because of  
75 stress associated with contraction/shrinkage during the solidification.

76 - *Extrusion:* The as-received cast ingot was machined into a rod having a 30 mm diameter and 20 mm  
77 length, which was then subjected to hot extrusion using a laboratory extrusion rig embedded in a servo-  
78 hydraulic testing frame having a load capacity of 350 kN. The hot extrusion was performed at 350 °C  
79 temperature and a ram speed of 0.1 mm/s to obtain an extruded rod with final diameter of 8 mm.

80 Electron backscatter diffraction (EBSD) was employed to characterise the microstructures produced with  
81 the different processing routes. The EBSD samples were prepared using standard mechanical grinding  
82 and polishing procedures. They were further polished using a colloidal alumina slurry solution. The  
83 microscope was operated at 20 kV and 4 nA current using different step sizes, depending on the  
84 microstructure characteristics (i.e., grain size). For each processing route, several EBSD maps were  
85 obtained using a FEI Quanta 3D FEG SEM/FIB instrument. For the as-cast condition, multiple samples  
86 were prepared from different parts of the annealed block to provide a good statistical representation of  
87 the microstructure throughout the thickness. For the hot rolled condition, two perpendicular cross  
88 sections were taken: one in the rolling direction and normal direction (RD-ND), and the other in the  
89 rolling direction and transverse direction (RD-TD) for microstructure characterization. EBSD was also  
90 conducted on two perpendicular cross sections of the extruded sample, namely parallel to the extrusion  
91 direction (ED-TD) and perpendicular to the extrusion direction (TD-ND). Roughly equal amounts of

92 EBSD data were collected from two perpendicular cross-sections for the rolled and extruded conditions  
93 to diminish the texture bias introduced in the measurement of the grain boundary plane distribution using  
94 the five-parameter characterization approach, as described below. The EBSD map parameters were  
95 summarised in Table 1 for different processing conditions. The EBSD average confidence index varied  
96 between 0.6 to 0.7 depending on the microstructure characteristics developed for different processing  
97 routines.

98 The characterization of grain boundary interfaces in polycrystalline materials requires five independent  
99 macroscopic parameters: three for lattice misorientation and two for the boundary plane orientation [6].  
100 The lattice misorientation is defined by Euler angles ( $\phi_1$ ,  $\Phi$ ,  $\phi_2$ ) or an angle/axis pair ( $\theta$ /[uvw]), which  
101 are defined using conventional EBSD analysis. Each boundary segment corresponds to the grain  
102 boundary trace on the surface plane. The only remaining parameter is the inclination of the boundary  
103 plane relative to the surface to fully determine the boundary plane orientation. If enough grain boundary  
104 traces are collected for a given angle/axis pair, the grain boundary plane distribution can be determined  
105 using a stereological approach [6]. Here, it is expected that each grain boundary line segment is  
106 orthogonal to its boundary plane normal. Therefore, all possible plane normals for a given boundary  
107 segment lie on a great circle perpendicular to it on a stereographic projection. By measuring multiple  
108 boundary segments with a fixed lattice misorientation, the most probable plane/s appears as peak/s in the  
109 distribution, while less probable ones are observed less frequently and can be removed as background  
110 [6].

111 The TexSEM Laboratories (TSL) software was used to acquire the EBSD data and perform the data post-  
112 processing. For grain boundary plane characterisation, boundary lines/traces were obtained from EBSD  
113 data after conducting several data post-processing functions in the TSL software, namely grain dilation  
114 clean-up, single orientation designation for each grain, and grain boundary reconstruction [12]. The  
115 clean-up routine was performed to minimize ambiguous data from the orientation map, which, on  
116 average, altered less than 4% of original data points. The grain boundary reconstruction function  
117 smoothed uneven boundaries using a boundary deviation limit of 2 times the step size to extract boundary  
118 segments for each processing condition. Owing to the low crystal symmetry in the hexagonal crystal  
119 structure (i.e., AZ31 Mg alloy), a minimum of 200,000 boundary line segments were collected for each  
120 processing routine (Table 1) to correctly measure the grain boundary plane distribution using the five-  
121 parameter characterisation approach [6]. The current measurement had a minimum resolution of  $10^\circ$ . The  
122 Atex post-processing software [23] was used to plot the overall texture at different conditions.

123

124

125

Table 1: EBSD condition of AZ31 alloy produced through different processing routes

Condition	Grain Size	Step Size	EBSD Area	Total Line segments
As-Cast	$154 \pm 5 \mu\text{m}$	$5 \mu\text{m}$	$2400 \times 2400 \mu\text{m}^2 \times 220$	209,220
Extruded	$3.9 \pm 0.6 \mu\text{m}$	$0.2 \mu\text{m}$	$128 \times 128 \mu\text{m}^2 \times 42$	407,172
Rolled	$5.9 \pm 1.1 \mu\text{m}$	$0.2 \mu\text{m}$	$183 \times 183 \mu\text{m}^2 \times 53$	390,178

126

127

**Results:**

128

129

130

131

132

133

134

135

136

137

138

The microstructure of the as-cast specimen after heat treatment was relatively coarse with equiaxed grains having an average size of  $154 \pm 5 \mu\text{m}$  (Fig. 1a). The heat treatment had removed any tension twins formed because of the shrinkage taking place during the solidification [24]. The misorientation angle distribution exhibited several maxima at the misorientation angle range of  $5\text{-}10^\circ$ ,  $30\text{-}35^\circ$ ,  $55\text{-}65^\circ$  and  $85\text{-}90^\circ$  (Fig. 2a). The distribution deviated somewhat from the ideal random distribution, even though the overall texture was relatively weak with an intensity of  $\sim 1.8$  multiples of a random distribution (MRD, Fig. 2). The misorientation axis distribution at the peak positions largely exhibited maxima at  $[0001]$ ,  $[11\bar{2}0]$  and/or  $[10\bar{1}0]$  (Fig. 2a). The misorientation axis distribution at  $10^\circ$  had a maximum at  $[0001]$  spreading towards  $[10\bar{1}0]$ . At  $30^\circ$ , the distribution displayed a maximum at  $[10\bar{1}0]$ . The misorientation axis distribution at  $65^\circ$  revealed a peak near the  $[11\bar{2}0]$  position. A single peak was also observed at  $[11\bar{2}0]$  for the misorientation axis distribution at  $90^\circ$  (Fig. 2a).

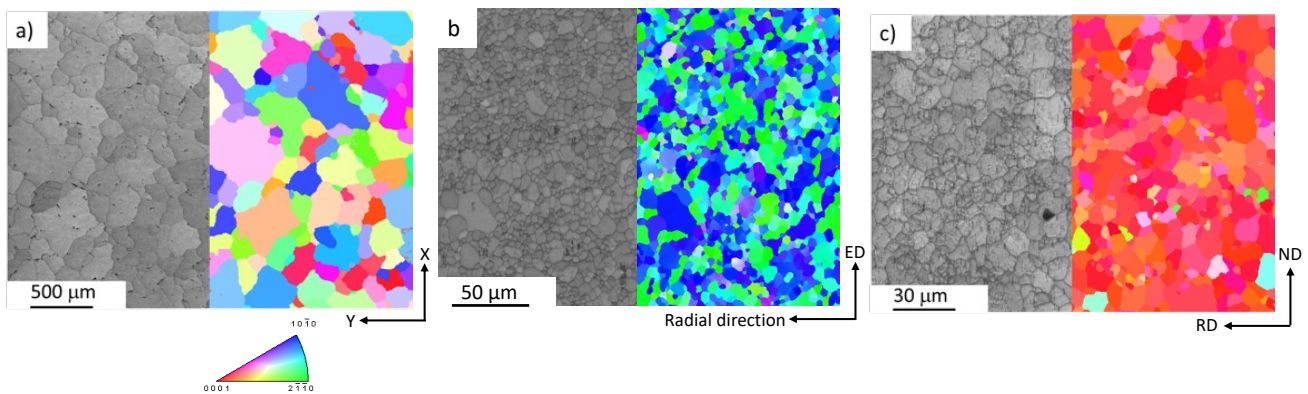


Figure 1: EBSD band contrast and their corresponding IPF images of AZ31 produced through different processing routes: a) as-cast, b) hot extrusion and c) hot rolling. The triangle inset in (a) is colour codes referring to the out of plane direction. X and Y in (a) are arbitrary directions, though the out of plane direction is parallel to the solidification direction. EX, RD and ND represent extrusion direction, rolling direction and normal direction, respectively.

139

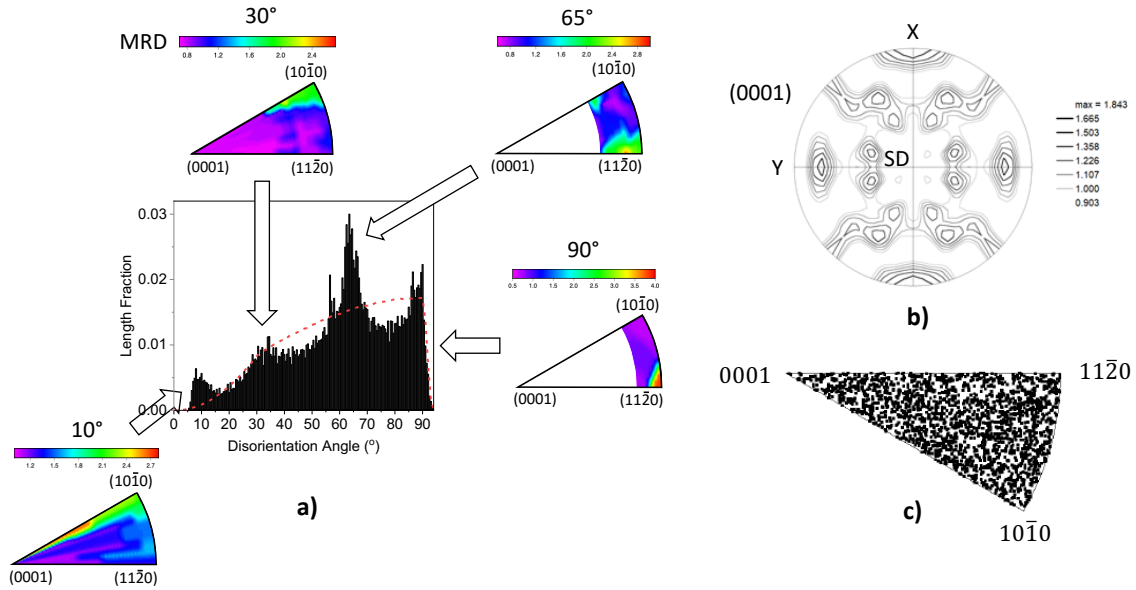


Figure 2: a) misorientation angle distribution of as-cast AZ31 alloy along with the misorientation axis distribution at the peaks. Dashed red line in (a) represents the random distribution of misorientation angle. The (0001) pole figure (b) reprinted with permission from reference [24] along with the inverse pole figure (c) of the as-cast AZ31 alloy. X and Y in (b) are arbitrary directions and SD represents the solidification direction. MRD represents multiples of a random distribution.

140 The hot extruded AZ31 alloy revealed fine equiaxed grains (i.e.,  $3.9 \pm 0.6 \mu\text{m}$ , Fig. 1b), displaying a  
 141 typical extrusion texture having  $\sim 6$  MRD intensity, where the extrusion direction is largely perpendicular  
 142 to the basal poles and parallel to the  $\{10\bar{1}0\}$  and  $\{11\bar{2}0\}$  poles (Fig. 3b). In turn, the inverse pole figure  
 143 showed a maximum at the  $[11\bar{2}0]$  direction spreading towards the  $[10\bar{1}0]$ , with  $\sim 5.9$  MRD intensity  
 144 (Fig. 3c). The misorientation angle distribution significantly deviated from the one expected for the ideal  
 145 random distribution, revealing two peaks at  $\sim 30^\circ$  and  $\sim 90^\circ$  (Fig. 3a). Interestingly, the misorientation  
 146 angle was nearly a plateau between  $\sim 45^\circ$  and  $\sim 85^\circ$ . The misorientation axis distribution largely clustered  
 147 at the  $[0001]$  for  $30^\circ$  and,  $[10\bar{1}0]$  and  $[11\bar{2}0]$  for  $90^\circ$  misorientation angle (Fig. 3a).

148 The specimen produced by hot rolling had small grain size of  $5.9 \pm 1.1 \mu\text{m}$  with an equiaxed morphology  
 149 (Fig. 1c). The sample displayed a strong basal texture, where the normal direction was parallel to the  
 150 basal plane, spreading by  $\sim 20^\circ$  towards the rolling direction and having  $\sim 8.8$  MRD intensity (Fig. 4b).  
 151 The inverse pole figure also exhibited a strong peak at  $[0001]$ , having an intensity of  $\sim 8.8$  MRD (Fig.  
 152 4c). The population of misorientation angles increased continuously up to  $30^\circ$ , beyond which it  
 153 progressively decreased up to a misorientation angle of  $\sim 85^\circ$ . Thereafter, the misorientation angle  
 154 displayed a rather weak peak at  $\sim 90^\circ$  (Fig. 4a). The corresponding misorientation axis distribution at  $30^\circ$   
 155 exhibited a somewhat diffuse peak at  $[0001]$  position, it was clustered at  $[11\bar{2}0]$  for  $90^\circ$  misorientation  
 156 angle (Fig. 4a).

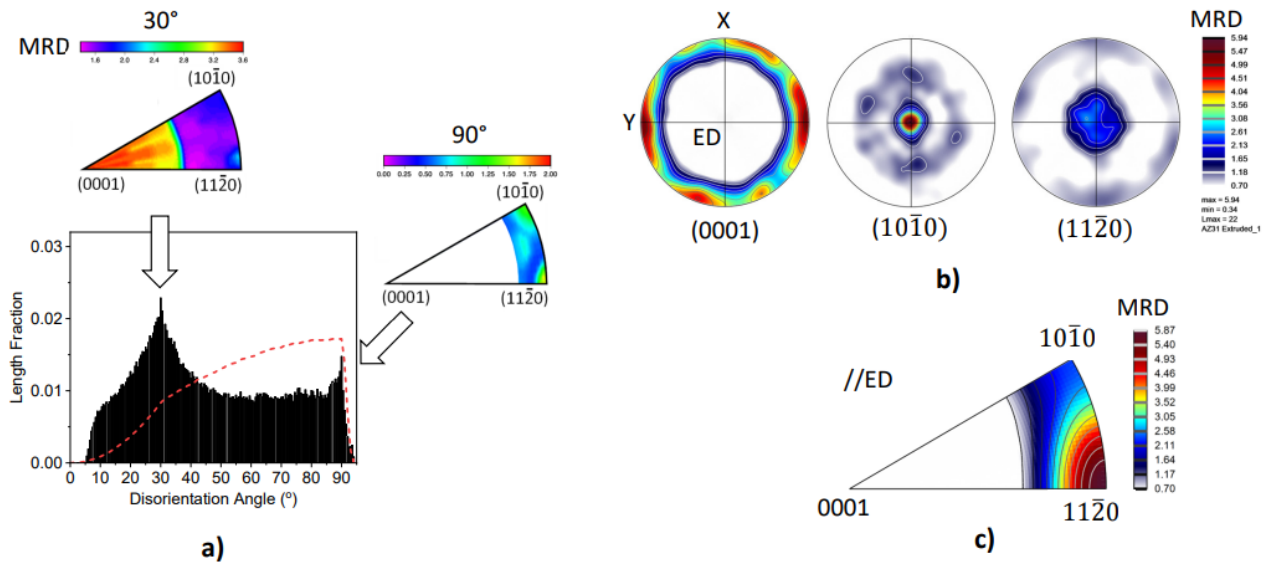


Figure 3: a) misorientation angle distribution of hot extruded AZ31 alloy along with the misorientation axis distribution at the peaks. Dashed red line in (a) represents the random distribution of misorientation angle. The pole figures (b) along with the inverse pole figure (c) of hot extruded AZ31 alloy. MRD represents multiples of a random distribution. ED is extrusion direction.

157

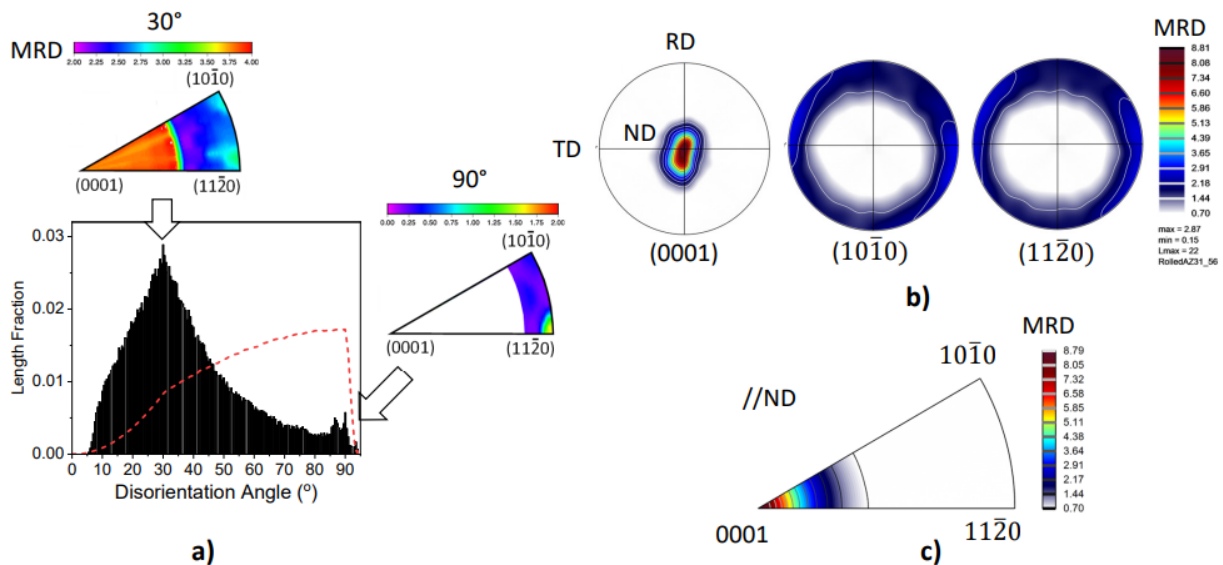


Figure 4: a) misorientation angle distribution of hot rolled AZ31 alloy along with the misorientation axis distribution at the peaks. Dashed red line in (a) represents the random distribution of misorientation angle. b) the pole figures (b) along with the inverse pole figure (c) of hot rolled AZ31 alloy. MRD represents multiples of a random distribution. RD, TD and ND are rolling direction, transverse direction and normal direction, respectively.

158

159 The grain boundary planes distribution was only drawn for  $30^\circ/[10\bar{1}0]$  and  $90^\circ/[11\bar{2}0]$  for the as-cast  
 160 AZ31 alloy, since those related to other lattice misorientations have been already presented in [24]. The  
 161 geometrically characteristic grain boundaries were also mapped for the corresponding lattice  
 162 misorientations to define the character of the relevant boundary using the toolbox defined in [25]. At

163  $30^\circ/[10\bar{1}0]$ , the grain boundary planes distribution showed a maximum close to the position of  $(\bar{1}2\bar{1}1)$   
 164 plane with an intensity of  $\sim 6.8$  MRD (Figs. 5a, d). For  $90^\circ/[11\bar{2}0]$ , the distribution displayed a peak  
 165 with an intensity of  $\sim 7.2$  MRD at the position of  $(01\bar{1}1)$  plane orientation with twist character,  
 166 considering an equivalent lattice misorientation outside of fundamental zone (Figs. 5c, g).

167 For the hot extruded condition, the grain boundary plane distribution at  $30^\circ/[0001]$  exhibited multiple  
 168 peaks with an intensity of  $\sim 5$  MRD at the positions of the  $\{11\bar{2}0\}$  and  $\{10\bar{1}0\}$  prism planes, which differ  
 169 by  $30^\circ$  about the  $[0001]$  misorientation axis (Figs. 5b, e). This suggests that it has  $(2\bar{1}\bar{1}0)//(10\bar{1}0)$   
 170 asymmetric tilt character, since the grain boundary planes are from distinct family. The grain boundary  
 171 planes at the  $90^\circ/[11\bar{2}0]$  and  $90^\circ/[10\bar{1}0]$  misorientations did not have maxima greater than 2.5 MRD  
 172 and were not considered significant to present.

173 For the hot rolled condition, the grain boundary plane distribution at  $30^\circ/[0001]$  misorientation showed  
 174 a peak at the position of  $(0001)$  with  $\sim 5.8$  MRD, suggesting pure twist character (i.e., the misorientation  
 175 axis and plane normal are parallel, Figs. 5b, f). However, the distribution at  $90^\circ/[11\bar{2}0]$  exhibited two  
 176 main peaks with  $\sim 5.1$  MRD intensity at the  $(1\bar{1}02)$  and  $(\bar{1}102)$  planes, having symmetric tilt character,  
 177 since both planes at the boundary belong to the same family (i.e.,  $(1\bar{1}02)//(\bar{1}102)$ , Figs. 5c, h).

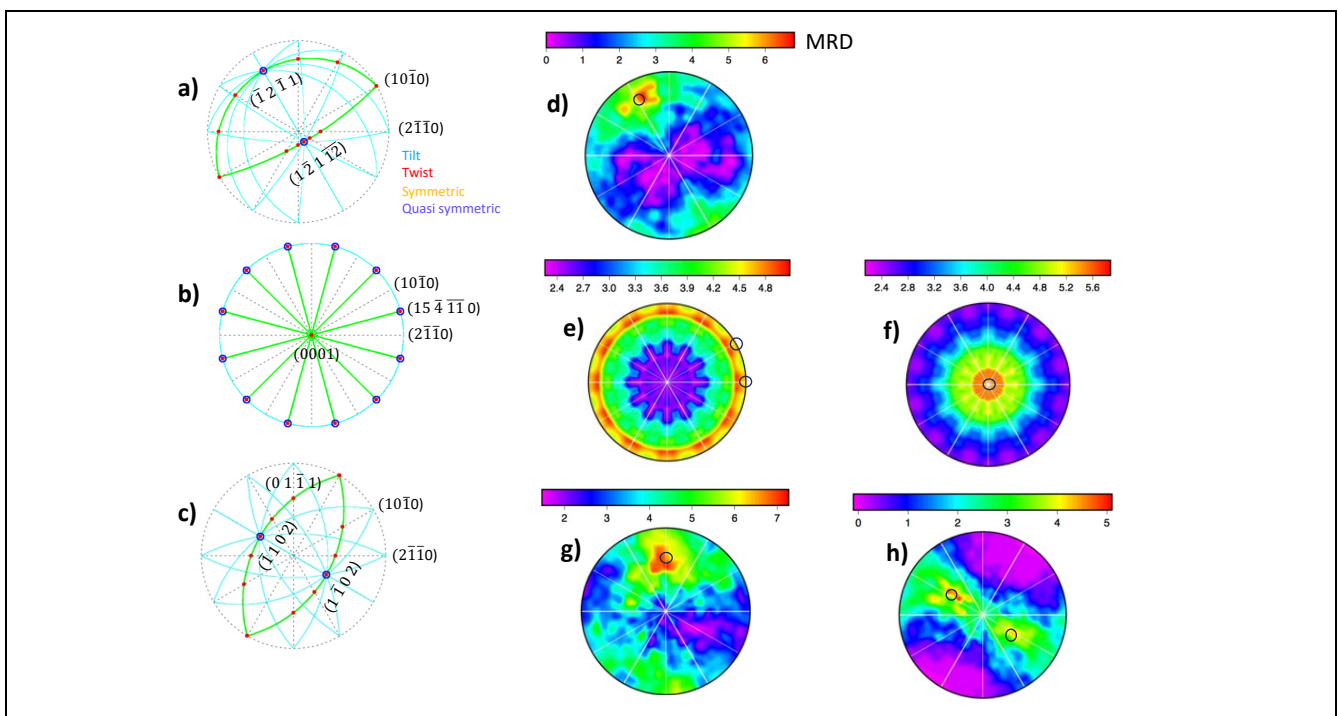


Figure 5: The calculated locations of the geometrically characteristic boundaries [25] for lattice misorientations of (a)  $30^\circ/[10\bar{1}0]$ , (b)  $30^\circ/[0001]$  and (c)  $90^\circ/[11\bar{2}0]$ . The distribution of grain boundary planes character for different lattice misorientations for microstructures produced through different processing routes: d)  $30^\circ/[10\bar{1}0]$ , as-cast, e)  $30^\circ/[0001]$ , hot extruded, f)  $30^\circ/[0001]$ , hot rolled, g)  $90^\circ/[11\bar{2}0]$ , as-cast, and h)  $90^\circ/[11\bar{2}0]$ , hot rolled. MRD represents multiples of a random distribution.

179 The grain boundary plane distribution, irrespective of misorientation, was plotted for all microstructures  
180 formed during the different processing routes (Fig. 6). It appeared that the processing condition  
181 significantly affected the distribution. For the as-cast condition, the highest intensity was at  $(10\bar{1}0)$  with  
182 1.07 MRD, spreading towards the  $(5\bar{2}\bar{3}0)$ . The minimum intensity was 0.93 MRD at  $(0001)$ . In general,  
183 the intensity difference was  $\sim 14\%$  between the maximum and minimum positions in the distribution,  
184 indicating a relatively weak anisotropic distribution (Fig. 6a).

185 For the hot extruded condition, the boundaries were largely terminated on  $\{hki0\}$  prismatic planes with  
186 a maximum of 1.45 MRD at the  $(11\bar{2}0)$  orientation, spreading towards the  $(10\bar{1}0)$  orientation (Fig. 6b).  
187 This confirms that the distribution of grain boundary plane orientations was anisotropic, because the  
188  $\{hki0\}$  prismatic plane population was 45% higher than anticipated in a random distribution.

189 For the hot rolled condition, the grain boundary plane distribution was significantly different compared  
190 with other conditions, displaying the highest intensity of 1.22 MRD at the  $(0001)$  basal plane orientation  
191 (Fig. 6c). The distribution was anisotropic, having the population of  $(0001)$  basal plane orientation 22%  
192 larger than expected from a random distribution. By contrast, the distribution exhibited a minimum at the  
193  $\{hki0\}$  prismatic planes.

194

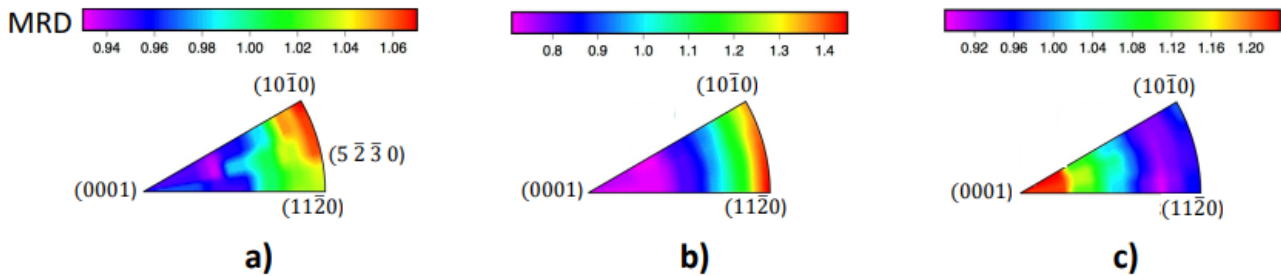


Figure 6: The grain boundary planes character distribution ignoring misorientation for AZ31 alloy produced through different processing routes: a) as-cast reprinted with permission from reference [24], b) hot extruded and c) hot rolled. MRD is multiples of random distribution.

195

## 196 Discussion:

197 The current result demonstrates that the grain boundary network (i.e., the distribution of misorientations  
198 and plane grain boundary orientations) is significantly affected by the processing route for AZ31 Mg  
199 alloy (Figs. 2-6). There are a wide range of parameters affecting the boundary network in polycrystalline  
200 materials, namely chemical composition [10, 11,14], phase transformation mechanism [11-13, 26], initial  
201 grain size [27], and crystallographic texture [13, 17-21]. The chemical composition and phase  
202 transformation mechanism can be excluded here, because the composition is similar for all different

203 processing routes and the material did not undergo any phase transformation during processing.  
 204 However, the grain size of the as-cast condition is much greater than others, although they are relatively  
 205 similar for the hot extruded and hot rolled conditions (Table 1), where they have distinct grain boundary  
 206 plane distributions (Fig. 6). This suggests that the grain size is not the most important factor determining  
 207 the grain boundary network in the current study. However, the overall orientation texture is significantly  
 208 different due to varying processing routes.

209 The overall texture significantly affects the population of grain boundaries in polycrystalline materials  
 210 [13, 17-21]. This was largely demonstrated for materials with the cubic crystal structure, where the  
 211 introduction of a given crystallographic fibre texture through the processing route promotes specific  
 212 boundary type/s at the expense of others [20, 21]. The current observation also suggests that altering the  
 213 material processing route leads to unique overall texture, which influences the grain boundary network  
 214 (Figs. 2-6). The overall texture characteristics depend on the deformation mode and alloying content (i.e.,  
 215  $c/a$  ratio) [28]. Hot extrusion leads to the enhancement of prism orientations, where the extrusion  
 216 direction is parallel to the  $\{hki0\}$  orientations (Fig. 3). However, the hot rolling promotes the (0001)  
 217 basal orientation (i.e., ND//(0001), Fig. 4).

218 In both the hot extrusion and hot rolling processes, there is a dominant peak at the position of  $\sim 30^\circ$  (Figs.  
 219 3-4). However, the misorientation angle distribution varies beyond  $30^\circ$ , depending on the processing  
 220 route. To investigate the influence of overall orientation texture on the misorientation angle distribution,  
 221 we utilised a similar approach recently used by our group to assess the role of  $\gamma$ -fibre and  $\theta$ -fibre texture  
 222 on the misorientation angle distribution in fully ferritic IF-steel [20] and fully austenitic Ni-30Fe alloy  
 223 [21]. Considering the  $c/a$  ratio of the AZ31 alloy (i.e., 1.6247 [29]), this is close to the ideal  $c/a$  ratio of  
 224 1.633, expected to largely produce the ND//(0001) fibre in rolling [30]. Here, 5000 orientations are  
 225 randomly selected along the ND//(0001) fibre, where these orientations have their  $\varphi_1$  and  $\varphi_2$  angles  
 226 arbitrarily designated, varying from  $0^\circ$  through  $360^\circ$ , with fixed  $\phi$  angle of  $0^\circ$  (Fig. 7a). The disorientation  
 227 angle resulted from the two orientations, located along the ND//(0001) fibre is calculated using the  
 228 Equation 1.

$$229 \quad \Delta g_{ij} = (O_m g_j)(O_l g_i)^{-1} \quad \text{Eq. 1}$$

230 where  $\Delta g_{ij}$  is disorientation angle and  $g_i$  and  $g_j$  are  $i$ th and  $j$ th orientation of every two adjacent sets,  
 231 respectively, both changing from 1 to 5000.  $O_l$  and  $O_m$ , in turn, represent the 12 hexagonal symmetry  
 232 operators for  $g_i$  and  $g_j$ . The disorientation refers to the minimum angle and is calculated from the set of  
 233 288 equivalent misorientations, considering switching symmetry. Here, it is assumed that the  
 234 hypothetical orientations intersect each other only one time throughout the calculation, with  $i$  equal or

235 smaller than  $j$ . Furthermore, the boundary formed from the intersection of every orientation pair has a  
 236 constant length for each calculated boundary. Hence, it does not influence the resultant disorientation  
 237 angle distribution. The distribution was discretised with a bin width of  $1^\circ$ . The resultant disorientation  
 238 angles display a uniform distribution, restricted in the range of  $0$  to  $30^\circ$ , which covers all distinguishable  
 239 rotation angles about the  $[0001]$  (Fig. 7a). This signifies that the manifestation of strong basal fibre  
 240 texture enhances the presence of all disorientation angles ranging from  $0^\circ$  to  $30^\circ$  with an equal  
 241 probability, resulting in a uniform/flat distribution. The result of this calculation significantly differs from  
 242 the current experimental measurement, where there is a maximum in the misorientation angle distribution  
 243 at  $30^\circ$  (Fig. 4a and 7a). This discrepancy could be due to the difference in the overall texture of the hot  
 244 rolled AZ31 alloy from the ideal basal fibre, where the peak was spread from the normal direction  
 245 towards the rolling direction by  $\sim 20^\circ$  (Fig. 4b). To synthetically generate the experimental texture, the  
 246 5000 hypothetical orientations are arbitrarily selected from Euler angles space of  $\varphi_1 = 0$  through  $360^\circ$ ,  $\phi$   
 247  $= 140^\circ$  through  $180^\circ$  and  $\varphi_2 = 0$  through  $360^\circ$ , so that the overall texture appears as an ellipse spread  $20^\circ$   
 248 towards RD. The calculated disorientation angle distribution shows a single peak at the  $30^\circ$  disorientation  
 249 angle, progressively reducing with the disorientation angle (Fig. 7b). This closely matches with the  
 250 measured experimental data (Fig. 4). The calculation was also performed for the material with a pole in  
 251 their overall texture elongated towards the TD direction, representing the materials with  $c/a < 1.633$  such  
 252 as Ti. The calculation exhibited a similar trend with a pronounced peak at  $30^\circ$  (Fig. 7c). A similar  
 253 disorientation angle distribution was also reported by others for different hexagonal materials (Zr [31],  
 254 Ti [32]) subjected to the hot rolling and/or recrystallisation.

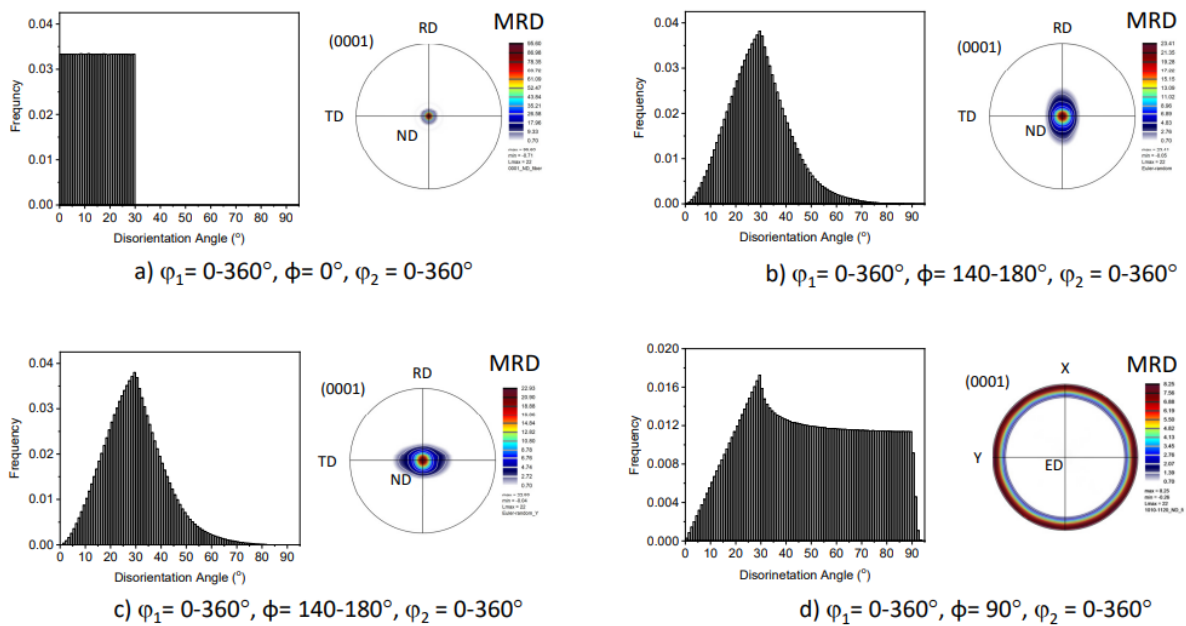


Figure 7: Disorientation angle distribution resulted from the impingement of each pair of 5000 synthetically chosen orientations within different Euler angles ranges and their corresponding (0001) pole figures.

255 To evaluate the influence of hot extrusion texture on the disorientation angle distribution, 5000  
256 hypothetical orientations are randomly chosen from the Euler angles space of  $\varphi_1 = 0$  through  $360^\circ$ ,  $\phi =$   
257  $90^\circ$  and  $\varphi_2 = 0$  through  $360^\circ$ . The calculated data exhibit a sharp increase in the disorientation angle up  
258 to  $30^\circ$  beyond which it reduces with the disorientation angle up to  $45^\circ$ . Afterwards, the distribution  
259 became flat up to  $90^\circ$ , where it sharply reduces (Fig. 7d). This closely matches the experimentally  
260 measured distribution, although some fluctuations appeared in the experimental result, which can be due  
261 to the deviation in the measured overall texture from the ideal assumed condition (Fig. 3).

262 The current observations also demonstrate that the grain boundary plane distribution is anisotropic (Fig.  
263 6), which is consistent with the other reports for a wide range of polycrystalline materials [4, 5, 33, 34].  
264 However, the extent of anisotropy and the distribution characteristics were significantly affected by the  
265 processing route. It has been demonstrated that an inverse relationship exists between the relative areas  
266 of grain boundaries and their energies for microstructures formed through normal grain growth, both in  
267 simulations [35-38] and experimental measurements [4, 5, 39, 40]. In fact, the grain boundaries which  
268 are frequently observed exhibit the least energy and vice versa. Here, the interplanar spacing (i.e.,  $d_{hkl}$ )  
269 of the boundary planes is employed as a proxy for the relative grain boundary energy [41, 42], due to a  
270 lack of information regarding the grain boundary energies of Mg alloys. Based on this model, a boundary  
271 consisting of planes with large interplanar spacing refers to a low energy boundary, as they are fairly flat  
272 and smooth with limited numbers of broken bonds. Therefore, they probably match better with the  
273 neighboring plane, consequently reducing repulsion forces at the boundary and lowering the grain  
274 boundary energy [41, 42]. By contrast, smaller interplanar spacings imply more broken bonds and  
275 rougher planes, which ultimately reduce the atomic density of boundary structure, leading to higher  
276 boundary energy. Table 2 listed the interplanar spacings of planes representing maxima in the  
277 distributions measured in the present work.

278 Interestingly, the link between the populations and the interplanar spacing does not follow a similar trend  
279 for all processing conditions. For the hot rolled condition, a direct correlation appears between the  
280 populations and the interplanar spacing, where the (0001) basal plane with the highest population has  
281 the largest interplanar spacing ( $2.6 \text{ \AA}$ ) among all boundary planes (Fig. 6c and Table 2). However, no  
282 direct trend is observed between populations and interplanar spacing for the as-cast and hot extruded  
283 conditions (Figs. 6a-b and Table 2). Here, the  $\{hki0\}$  prismatic planes (e.g.,  $(10\bar{1}0)$ ,  $(5\bar{2}\bar{3}0)$  and  $(11\bar{2}0)$ )  
284 are the most frequent planes, though their interplanar spacings are lower than for the (0001) basal plane  
285 with minimum population (Table 2). This confirms that the grain boundary energy is not the most  
286 important factor determining the grain boundary plane distribution when the processing route leaves an  
287 imprint on the microstructure.

288

Table 2: The interplanar spacings ( $d_{hkl}$ ) for different planes observed in Figures 5 and 6.

Plane Orientation	Interplanar Spacing ( $\text{\AA}$ )
(0001)	2.60
(10 $\bar{1}$ 0)	1.86 or 0.93 <sup>^</sup>
(11 $\bar{2}$ 0)	1.6
(5 $\bar{2}$ $\bar{3}$ 0)	0.43 or 0.21 <sup>^</sup>
( $\bar{1}$ 2 $\bar{1}$ 1)	0.77
(01 $\bar{1}$ 1)	2.44 or 0.41 <sup>^</sup>
(1 $\bar{1}$ 02)	1.27 or 0.63 <sup>^</sup>
( $\bar{1}$ 102)	1.27 or 0.63 <sup>^</sup>

289

<sup>^</sup> Considering the structure factor where the plane passing through an additional atom [43].

290

291 The main difference among these microstructures is the processing condition, which leads to different  
 292 overall textures. There is ample evidence that the overall texture has a direct impact on the relative areas  
 293 of grain boundaries [20,21,44]. For example, the promotion of  $\gamma$ -fibre (i.e., (111)//*ND*) in IF steel with  
 294 a fully ferritic structure enhances the boundaries with a (111) plane orientation, having a greater energy  
 295 compared with the (110) close packed plane orientation (i.e., low energy plane) [20]. Similarly, the  
 296 increase in the strength of  $\theta$ -fibre (i.e., (001)//*ND*) in a Ni-30Fe alloy leads to the enhancement of  
 297 boundaries terminated at (001) rather than the (111) close packed plane in materials with the face  
 298 centred cubic structure [21]. This is similar to the current observation, where the grain boundary plane  
 299 distribution is closely matched with the overall texture for both hot extrusion and hot rolling conditions.  
 300 For example, the hot extrusion condition enhances the relative areas of boundaries that terminate at  
 301  $\{hki0\}$  prismatic plane orientations (Figs. 3c, 6b). A similar distribution was observed for  $\alpha$ -Ti, though  
 302 the anisotropy was relatively weak [45]. In terms of the hot rolling condition, the promotion of the (0001)  
 303 basal fibre leads to the (0001) basal planes, which coincide with the low energy position based on the  
 304 interplanar spacing criterion (Figs. 4c, 6c and Table 2). However, in this case the large relative areas of  
 305 (0001) planes are a consequence of the processing and are not likely to be energetically driven. Regarding  
 306 the as-cast condition, a relatively stronger  $\{hki0\}$  prismatic plane orientations in the distribution (Fig. 6a)  
 307 could be explained due to the existence of remaining columnar grains, developed during the growth of  
 308 dendrites with their six secondary arms being along the  $\langle 11\bar{2}0 \rangle$  direction upon solidification [46].  
 309 However, the orientations of lateral columnar surfaces are expected to be perpendicular to the  $\langle 11\bar{2}0 \rangle$   
 310 growth direction (i.e.,  $\{1\bar{1}00\}$  and (0001)). This is contradicted by the observation that the grain

311 boundary plane distribution maximizes at  $\{1 \bar{1}0 0\}$ , but not (0001) [24].

312 The current result demonstrates that the hot rolling condition has the highest population of low angle  
313 grain boundaries among different processing routes (Figs. 2-4). Based on the simulation result presented  
314 in [8], it is expected that the grain boundary network developed in AZ31 alloy produced through the hot  
315 rolling is more prone to the mechanical twinning nucleation on grain boundaries, considering the link  
316 between grain boundary character (i.e., misorientation angle of  $<10^\circ$  [8]) and mechanical twinning.

### 317 **Conclusions:**

318 In the current investigation, the role of processing route (i.e., chill casting, hot extrusion and hot rolling)  
319 on the overall orientation texture and the characteristics of grain boundary network was investigated for  
320 an AZ31 alloy. The observations lead to the following conclusions:

- 321 1) The processing route altered the overall texture, revealing random texture in the as-cast condition,  
322 although the  $\{hki0\}$  prism and the (0001) basal textures were dominant after hot extrusion and  
323 hot rolling, respectively.
- 324 2) The change in the overall texture appeared to control the misorientation angle distribution, where  
325 the as-cast condition displayed a relatively random distribution. However, the distribution  
326 deviated significantly from the random case for both the hot extruded and hot rolled conditions,  
327 displaying pronounced peaks at  $\sim 30^\circ$ . Computed misorientation angle distributions based on  
328 simulations confirmed the role of texture in determining these distributions.
- 329 3) The distribution of grain boundary planes was somewhat anisotropic for the as-cast condition,  
330 showing stronger  $\{hki0\}$  prismatic plane orientations. In comparison, the anisotropy became  
331 much stronger for both hot extruded and hot rolled materials.
- 332 4) The characteristics of overall texture appeared to strongly influence the relative areas of grain  
333 boundary planes. The basal texture in the hot rolled condition enhanced the occurrence of the  
334 (0001) basal plane orientation, but the  $\{hki0\}$  prismatic plane orientations appeared more  
335 frequently in the hot extruded material, despite having a relatively higher energy than the (0001)  
336 basal plane.

### 337 **Acknowledgements:**

338 Deakin University's Advanced Characterisation Facility is acknowledged for use of the EBSD  
339 instruments.

### 340 **Conflict of Interest Statement**

341 On behalf of all authors, the corresponding author states that there is no conflict of interest.

342

343 **References**

- 344 [1] M.H. Yoo, Slip, twinning, and fracture in hexagonal close-packed metals. *Metall. Trans. A* 12 (1981),  
345 pp. 409–418.
- 346 [2] M.A. Meyers, O. Vohringer, and V.A. Lubarda, The onset of twinning in metals: A constitutive  
347 description. *Acta Mater.* 49 (2001), pp. 4025-4039.
- 348 [3] L. Capolungo, P.E. Marshall, R.J. McCabe, I.J. Beyerlein, and C.N. Tome', Nucleation and growth  
349 of twins in Zr: A statistical study. *Acta Mater.* 57 (2009), pp. 6047-6056.
- 350 [4] H. Beladi, N.T. Nuhfer, and G.S. Rohrer, The five-parameter grain boundary character and energy  
351 distributions of a fully austenitic high-manganese steel using three dimensional data. *Acta Mater.*, 70  
352 (2014), pp. 281-289.
- 353 [5] H. Beladi and G.S. Rohrer, The relative grain boundary area and energy distributions in a ferritic steel  
354 determined from three-dimensional electron backscatter diffraction maps, *Acta Mater.*, 61 (2013), pp.  
355 1404-1412.
- 356 [6] G.S. Rohrer, D.M. Saylor, B.E. Dasher, B.L. Adams, A.D. Rollett and P. Wynblatt, The distribution  
357 of internal interfaces in polycrystals, *Zeitschrift für Metallkunde*, 95 (2004), pp. 197-214.
- 358 [7] V. Shterner, I.B. Timokhina, A.D. Rollett, H. Beladi, The role of grain orientation and grain boundary  
359 characteristics in the mechanical twinning formation in a high manganese twinning-induced plasticity  
360 steel, *Metall. and Mater. Trans. A*, 49 (2018), pp. 2597-2611
- 361 [8] I.J. Beyerlein, L. Capolungo, P.E. Marshall, R.J. McCabe, and C.N. Tome', Statistical analyses of  
362 deformation twinning in magnesium, *Philos. Mag.*, 90 (2010), pp. 2161–90.
- 363 [9] T. Watanabe, Grain boundary design for new materials, *Trans. Japan Inst. Metals* 27 (1986) 73.
- 364 [10] V. Randle, Mechanism of twinning-induced grain boundary engineering in low stacking-fault energy  
365 materials, *Acta Mater.*, 47 (1999), pp. 4187-4196.
- 366 [11] E. Farabi, V. Tari, P.D. Hodgson, G.S. Rohrer, H. Beladi, On the grain boundary network  
367 characteristics in a martensitic Ti–6Al–4V alloy, *J. Mater. Sci.*, 55 (2020), pp. 15299-15321.
- 368 [12] H. Beladi, G.S. Rohrer, A.D. Rollett, V. Tari and P.D. Hodgson, The distribution of intervariant  
369 crystallographic planes in a lath martensite using five macroscopic parameters, *Acta Mater.*, 63 (2014),  
370 pp. 86-98.
- 371 [13] H. Beladi, G.S. Rohrer, The role of thermomechanical routes on the distribution of grain boundary  
372 and interface plane orientations in transformed microstructures, *Metall. and Mater. Trans. A*, 48 (2017),  
373 pp. 2781-2790.
- 374 [14] V. Govindaraj, E. Farabi, S. Kada, P.D. Hodgson, R. Singh, G.S. Rohrer, H. Beladi, Effect of  
375 manganese on the grain boundary network of lath martensite in maraging stainless steels, *J. Alloys and*  
376 *Compounds*, 886 (2021) 161333.
- 377 [15] A. Mirzaei, R. Ghaderi, P.D. Hodgson, X. Ma, G.S. Rohrer and H. Beladi, The influence of parent  
378 austenite characteristics on the intervariant boundary network in a lath martensitic steel, *J. Mater. Sci.*,  
379 57 (2022), pp. 8904-8923.
- 380 [16] A. Mirzaei, P.D. Hodgson, X. Ma, V. Peterson, E. Farabi, G.S. Rohrer, H. Beladi, The role of parent  
381 austenite grain size on the variant selection and intervariant boundary network in a lath martensitic steel,  
382 *Mater. Sci. and Eng. A*, 889 (2024) 145793.

383 [17] H. Beladi, E. Farabi, P.D. Hodgson, M.R. Barnett, G.S. Rohrer and D. Fabijanic, Microstructure  
384 evolution 316L stainless steel using solid-state additive friction stir deposition, *Phil. Mag.*, 102 (2022),  
385 pp. 618-633.

386 [18] D.A. West, B.L. Adams, Analysis of orientation clustering in a directionally solidified nickel-based  
387 ingot, *Metall. Mater. Trans. A*, 28 (1997), pp. 229-236.

388 [19] R.E. Garcia, M.D. Vaudin, Correlations between crystallographic texture and grain boundary  
389 character in polycrystalline materials, *Acta Mater.*, 55 (2007), pp. 5728-5735.

390 [20] H. Beladi, V. Tari, A.D. Rollett and G.S. Rohrer, The influence of  $\gamma$ -fibre texture on grain boundary  
391 character distribution of an IF-steel, *Scripta Mater.*, 222 (2023) 115042.

392 [21] H. Beladi, Q. Chao, V. Tari, A.D. Rollett and G.S. Rohrer, The influence of processing and texture  
393 on the grain boundary character distribution of an austenitic Ni-30Fe alloy, *Mater. Charac.*, 197 (2023)  
394 112708.

395 [22] Y. Wu and R. Zhu, Effect of Rolling Temperature on the Microstructure and Mechanical Properties  
396 of AZ31 Alloy Sheet Processed through Variable-Plane Rolling. *J. Mater. Eng. and Perfor.*, 28 (2019)  
397 6182-6191.

398 [23] B. Beausir and J.-J. Fundenberger, Analysis tools for electron and X-ray diffraction, ATEX -  
399 software, [www.atex-software.eu](http://www.atex-software.eu), Université de Lorraine-Metz, 2017.

400 [24] H. Beladi, A. Ghaderi and G.S. Rohrer, Five-parameter grain boundary characterization of randomly  
401 textured AZ31 Mg alloy, *Phil. Mag.*, 100 (2020) 456-466.

402 [25] K. Glowinski, A. Morawiec, A toolbox for geometric grain boundary characterization, in: *Proc. 1st*  
403 *Int. Conf. 3D Mater. Sci*, Springer, Cham, 2012, pp. 119-124.

404 [26] N. Haghdadi, P. Cizek, P.D. Hodgson, V. Tari, G.S. Rohrer, H. Beladi, Effect of ferrite-to-austenite  
405 phase transformation path on the interface crystallographic character distributions in a duplex stainless  
406 steel, *Acta Mater.*, 145 (2018), pp. 196-209.

407 [27] T. Liu, S. Xia, H. li, B. Zhou, Q. Bai, C. Su, Z. Cai, Effect of initial grain sizes on the grain boundary  
408 network during grain boundary engineering in Alloy 690, *J. Mater. Res.*, 28 (2013), pp. 1165-1176.

409 [28] G. Gottstein and T. Al Samman, Texture development in pure Mg and Mg alloy AZ31, *Materials*  
410 *Science Forum* 495-497 (2005) 623-632.

411 [29] T.H. Rriyanto, A. Insani, R. Muslih, Bharoto, Texture analysis on the AZ31 magnesium alloy using  
412 neutron diffraction method, *IOP conf. Series: J. of Physics*, 1436 (2020) 012061.

413 [30] Y.N. Wang, J.C. Huang, Texture analysis in hexagonal materials, *Mater. Chem. and Phys.*, 81  
414 (2003), pp. 11-26.

415 [31] N. Bozzolo, F. Gerspach, G. Sawina, F. Wagner, Accuracy of orientation function determination  
416 based on EBSD data- A case study of a recrystallized low alloyed Zr sheet, *J. of Microscopy*, 227 (2007),  
417 pp. 275-283.

418 [32] N. Bozzolo, N. Dewobroto, T. Grosdidier, F. Wagner, Texture evolution during grain growth in  
419 recrystallized commercially pure titanium, *Mater. Sci. and Eng. A*, 397 (2005), pp 346-355.

420 [33] D.M. Saylor, B. Dasher, Y. Pang, H.M. Miller, P. Wynblatt, A.D. Rollett, and G.S. Rohrer, Habits  
421 of grains in dense polycrystalline solids, *J. the Amer. Ceramic Soc.*, 87 (2004), pp. 724-726.

422 [34] H. Beladi, G.S. Rohrer, The distribution of grain boundary planes in interstitial free steel, *Metall. &*  
423 *Mater. Trans. A*, 44 (2013), pp. 115-124.

- 424 [35] J. Gruber, D.C. George, A.P. Kuprat, G.S. Rohrer, A.D. Rollett, Effect of anisotropic grain boundary  
425 properties on grain boundary plane distributions during grain growth, *Scripta Mater.*, 53 (2005), pp. 351-  
426 355.
- 427 [36] G.S. Rohrer, J. Gruber, A.D. Rollett, A model for the origin of anisotropic grain boundary character  
428 distributions in polycrystalline materials, in *Applications of Texture Analysis*, in *Ceramic transactions*  
429 of applications of texture analysis, A.D. Rollett, eds., Hoboken, NJ: John Wiley, vol. 201, 2009, pp. 343-  
430 54.
- 431 [37] J. Gruber, G.S. Rohrer, A.D. Rollett, Misorientation texture development during grain growth. Part  
432 II: Theory, *Acta Mater.*, 58 (2010), pp. 14-19.
- 433 [38] J.D. Nino, O.K. Johnson, Influence of grain boundary energy anisotropy on the evolution of grain  
434 boundary network structure during 3D anisotropic grain growth, *Comp. Mater. Sci.*, 217 (2023), pp.  
435 111879.
- 436 [39] S.J. Dillon, G.S. Rohrer, Characterization of the grain boundary character and energy distributions  
437 of Yttria using automated serial sectioning and EBSD in the FIB, *J. Amer. Ceramic Soc.*, 92 (2009), pp.  
438 1580-1585.
- 439 [40] J. Li, S.J. Dillon, G.S. Rohrer, Relative grain boundary area and energy distributions in nickel, *Acta*  
440 *Mater.*, 57 (2009), pp. 4304-4311.
- 441 [41] D. Wolf, Correlation between structure, energy, and ideal cleavage fracture for symmetrical grain  
442 boundaries in fcc metals, *J. Mater. Research*, 5 (1990), pp. 1708-1730.
- 443 [42] C.S. Kim, G.S. Rohrer, Geometric and crystallographic characterization of WC surfaces and grain  
444 boundaries in WC-Co composites, *Interface Sci.*, 12 (2004), pp. 19-27.
- 445 [43] Q. Fan, A new method of calculating interplanar spacing: the position-factor method, *J. Applied*  
446 *Crystall.*, 45 (2012), pp.1303-1308.
- 447 [44] F. Heidelbach, H. R. Wenk, S. R. Chen, J. Pospiech, S. I. Wright, Orientation and misorientation  
448 characteristics of annealed, rolled and recrystallized copper, *Mater. Sci. Eng. A*, 215 (1996), pp. 39-49.
- 449 [45] M. N. Kelly, K. Glowinski, N.T. Nuhfer, G.S. Rohrer, The five parameter grain boundary character  
450 distribution of  $\alpha$ -Ti determined from three-dimensional orientation data, *Acta Mater.*, 111 (2016), pp. 22-  
451 30.
- 452 [46] K. Pettersen, N. Ryum, Crystallography of directionally solidified magnesium alloy AZ91. *Metall.*  
453 *Mater. Trans. A*, 20 (1989), pp. 847-852.